



Investigation of a Morphable Parawing for Unmanned Aerial Vehicle Application

Lance W. Traub* and Sho Okayama†
Embry-Riddle Aeronautical University, Prescott, Arizona 86301

DOI: 10.2514/1.C034557

A low-speed wind-tunnel investigation is presented characterizing the performance of dual-lobed parawings. Parawings are conically shaped geometries that possess significant washout and camber variation across the span. A series of models with a planar leading-edge sweep of 55 deg increasing to 65 deg to form the parawing canopy were tested. Asymmetric wing tests were also conducted to explore the ability of the configurations to generate moments suitable for roll control. The results indicate a significant reduction in lift with increasing wing slackness stemming from both a reduction in the lift curve slope and positive shift in the zero-lift angle of attack. The angle of attack for zero lift is shown to correlate strongly with the peak lobe height. Asymmetric wing setting showed the generation of rolling moments comparable in magnitude with those produced by traditional ailerons. Numerical simulation indicated that a freely available lifting-surface theory application is able to accurately simulate the performance of the parawing geometry.

Nomenclature

b	= span measured from keel
C_A	= attainable axial force coefficient
C_D	= drag coefficient
C_L	= lift coefficient
C_l	= rolling moment coefficient
C_m	= pitching moment coefficient
C_n	= yawing moment coefficient
C_Y	= side force coefficient
c	= chord
c_{root}	= root chord
k	= constant
l	= projected half-length of trailing edge
r	= length
S_p	= slackness parameter
s	= length, arc length
x, y, x', y'	= axis coordinates
x_k	= keel length
z	= vertical coordinate or height
$z_{c-\max}$	= maximum local camber
α	= angle of attack
δ_a	= aileron deflection angle
Λ	= leading-edge sweep angle
σ	= standard deviation
ϕ	= angle from keel

Subscripts

arc	= length of inflated trailing edge
arc-circ	= length of inflated trailing edge assuming circular arc geometry
LH	= left hand
max	= maximum
min	= minimum
n	= normal
RH	= right hand
TE	= trailing edge

ZL	= zero lift
0	= planar

I. Introduction

UNMANNED aerial vehicles (UAVs) have significantly expanded the configuration options available to the aircraft designer. Elimination of the complexity of human occupation promotes the design of flight vehicles with nonconventional or innovative geometry. The ability to “morph” (a somewhat generic term that generally encompasses alteration of an aircraft’s shape to augment performance and/or effect flight control) is also readily implemented at the scale of UAVs. Morphing encompasses aircraft geometric variations including sweep, telescoping wings, folding or rotating wings, variable camber, and twist [1–7]. Structural manipulation may be achieved through various electrically based film or wire actuators as well as torque rods in conjunction with a flexible- or multiple-hinged structure [1]. Pneumatics may also be employed for camber variation or wing deployment/telescoping. Most of these mechanisms are comparatively complicated and rely on new or unproven technology for actuation. Jacob and Smith [7] suggested that a primary benefit of morphing for small UAVs might be in the context of compact storage when not in use. Typical morphing mechanisms are mechanical wing folding and inflatable structures. As noted [7], most of these design options have issues in terms of complexity, scalability, weight, and leakage.

In the context of a small UAV, an enabling technology that simplifies design, promotes robustness and portability, and extends the flight envelope would be advantageous. Small UAVs fly in an environment where turbulence levels could be high and collisions with obstacles may be likely. Studied for possible use for atmospheric re-entry vehicles, parawings [8–16] are self-inflating delta-wing-shaped geometries commonly used in hang gliders. The wing typically consists of leading-edge tubes around which flexible [Mylar cloth, synthetic sailcloth (i.e., Dacron)] cloth is attached. The leading-edge tubing is in turn attached to a central keel. Cross braces are also commonly used to make the structure more rigid. Most parawings consist of a canopy formed from two self-inflating lobes. Studies of parawings have investigated the impact of sweep, leading-edge attachment, and lobe design [9,11,12,16]. Lobes are commonly assumed to be circular or parabolic in a cross-sectional shape.

Parawing simulation has encompassed empirical correlation or extended lifting line theory [12,14–16]. Application of Pankhurst’s method [17] and Weissinger’s method [18,19] to model the camber, angle of attack, and twist has shown good agreement with cylindrical but not conically shaped parawing canopies [20]. NASA-type parawings (implying equal wing leading edge and keel length coupled with high slackness, indicating a large peak lobe height) are

Received 10 May 2017; revision received 3 October 2017; accepted for publication 16 January 2018; published online 12 March 2018. Copyright © 2018 by the authors. Published by the American Institute of Aeronautics and Astronautics, Inc., with permission. All requests for copying and permission to reprint should be submitted to CCC at www.copyright.com; employ the ISSN 0021-8669 (print) or 1533-3868 (online) to initiate your request. See also AIAA Rights and Permissions www.aiaa.org/randp.

*Professor, Aerospace Engineering Department. Senior Member AIAA.

†Undergraduate Student, Aerospace Engineering Department. Student Member AIAA.

Table 1 99.7% Uncertainty intervals for force and moment coefficients

α , deg	C_D	C_Y	C_L	C_I	C_m	C_n
High	0.00298	0.00316	0.00739	0.00103	0.00113	0.00160
Low	0.00014	0.00048	0.00034	0.00003	0.00007	0.00003

not amenable to analysis using the methods described in [14–16], promulgating the lifting-line-based theory of Bass and Bertin [12]. Experimental data [11], supported by theory [12], indicates that increasing the slackness of the canopy (by increasing the leading-edge sweep angle) shifts the angle of attack for zero lift increasingly positive and reduces the lift curve slope. Stall angles of over 40 deg have been reported [11]. Conical-type parawings are (minimum) angle-of-attack limited due to flutter or collapse of the canopy facilitated by a loss of outboard loading [12]. A cylindrical-type parawing has the benefit of sustaining loading at low angles of attack [20]; consequently, they can operate at lower angles of attack than conical-type parawings but generally stall at a lower angle of attack than a conical geometry. A cylindrical-type parawing geometry is less amenable geometrically to leading-edge sweep variations, as irregularities in the canopy shape may occur.

A UAV equipped with a parawing could easily be collapsible (for transport and storage) through rotation of the wing leading edge to be coincident with the fuselage. The parawing design itself is naturally stall resistant, reducing sensitivity to atmospheric turbulence. Employment of a rigid but flexible material (e.g., a carbon-fiber tube) for the leading-edge tube would make it impact tolerant (especially if implemented in conjunction with a pusher propeller-type design). Differential rotation of the leading edge to change wing sweep may also prove suitable for lateral control. Consequently, this study represents an initial exploration of the performance and behavior of a two-lobed parawing and, as such, should be regarded as a proof of concept but not physical implementation. A series of NASA-type geometry parawings were tested based on a planar 55 deg leading-edge sweep diamond wing. The effect of symmetric and asymmetric sweep was examined using force and moment measurements. The experimental data were compared to simulations using a freely available vortex lattice code to explore whether such software is capable of accurate modeling of this type of geometry.

II. Equipment and Procedure

Wind-tunnel tests were conducted in Embry-Riddle Aeronautical University's 0.6096 by 0.6096 m blower wind tunnel. Force and

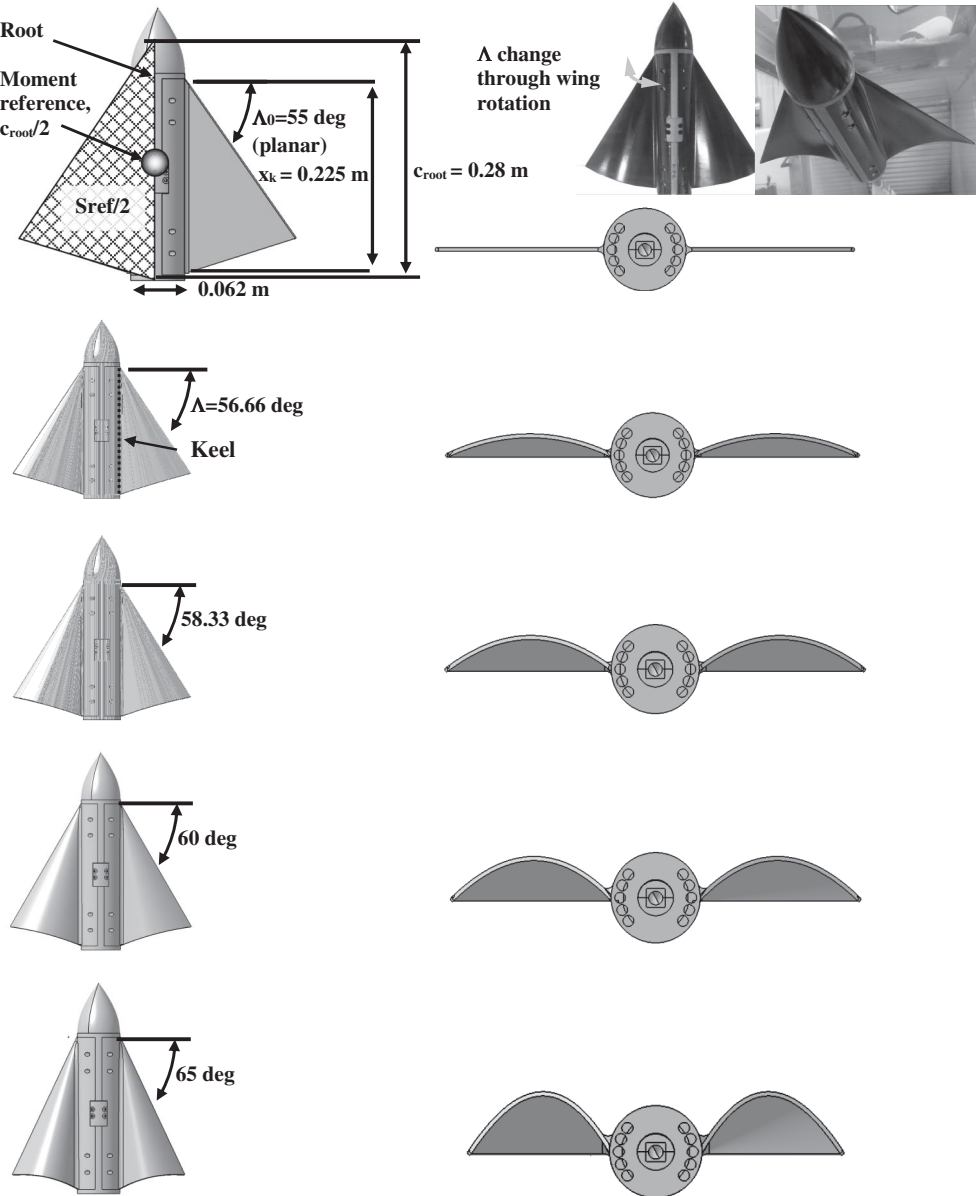


Fig. 1 Model geometric details.

moment measurements were taken with a six-component NK Biotechnical sting balance. Output voltages from the balance were digitized using a 16 bit analog-to-digital converter. Each presented data point is the average of 5000 samples. Repeated data measurements were used to calculate the 99.7% uncertainty intervals that are presented in Table 1, i.e., there is a 99.7% probability that the true value will lie between the calculated average and \pm the uncertainty interval. The uncertainty interval was estimated as $3\sigma/(5000)^{1/2}$. The uncertainty increases at higher angles of attack because the standard deviation is larger. Tests were conducted at a freestream velocity of 30 m/s, at which the measured turbulence intensity was 0.24%. Application of calibration weights indicated a worst-case accuracy for force and moment coefficients of 0.003 and 0.002 at the test velocity. The angle of attack was measured using a Midori sensor mounted on the sting balance, yielding a setting accuracy within 0.1 deg. Wall corrections were not employed due to the comparative nature of the tests and the moderate size of the models (worst-case blockage of less than 6%).

The wind-tunnel models were designed using a CAD package and were rapid prototyped, yielding acrylonitrile butadiene styrene models as shown in Fig. 1. The model consisted of a central cylindrical body onto which wing clamshells were attached. The nose cone of the body was that of a modified ogive. Body sizing was based on the requirement to accommodate the sting balance, as well as to provide a realistic volume if scaled for battery and motor accommodation to be a functional UAV. The planar wing (which

represented the baseline) had a leading-edge sweep angle of $\Lambda_0 = 55$ deg, yielding $AR = 2.8$. An increase in this angle (implying a greater slackness of the lobe) through rotation of the leading edge then generated the parawing geometry; consequently, the canopy consisted of two lobes. Leading-edge sweep angles of 56.66, 58.33, 60, and 65 deg were also manufactured; see Fig. 1. The reference area for all tests (Fig. 1) was that of the planar delta ($\Lambda_0 = 55$ deg) extended to the centerline, such that the root chord was 0.28 m. This form of nondimensionalizing is typical in parawing testing [11,12,20] and allows comparative assessment of the actual forces and moments generated. Based on this characteristic length (0.28 m), the test Reynolds number Re was 524,000. To be consistent with other studies, the keel was defined as that constituting the chord at the root of the wing and was $x_k = 0.225$ m for the test models (and was equal to the leading-edge length for all wings). The wing "skin" was 0.0031 m thick, giving a thickness-to-root chord of 1.2%. The wing's leading-edge profile was circular. All moments were taken about the midroot chord of the planar geometry, as indicated in Fig. 1. The pitching moment was nondimensionalized by the root chord (0.28 m), whereas the yawing and rolling moment were reduced by the total (i.e., including the diameter of the fuselage) wing span of the planar wing ($\Lambda_0 = 55$ deg).

Asymmetric tests, conducted to explore the potential for generating rolling moments, were implemented using a planar left-hand wing, while right-hand-side clamshells with 56.66 to 65 deg leading-edge sweep were sequentially attached. For the purposes of

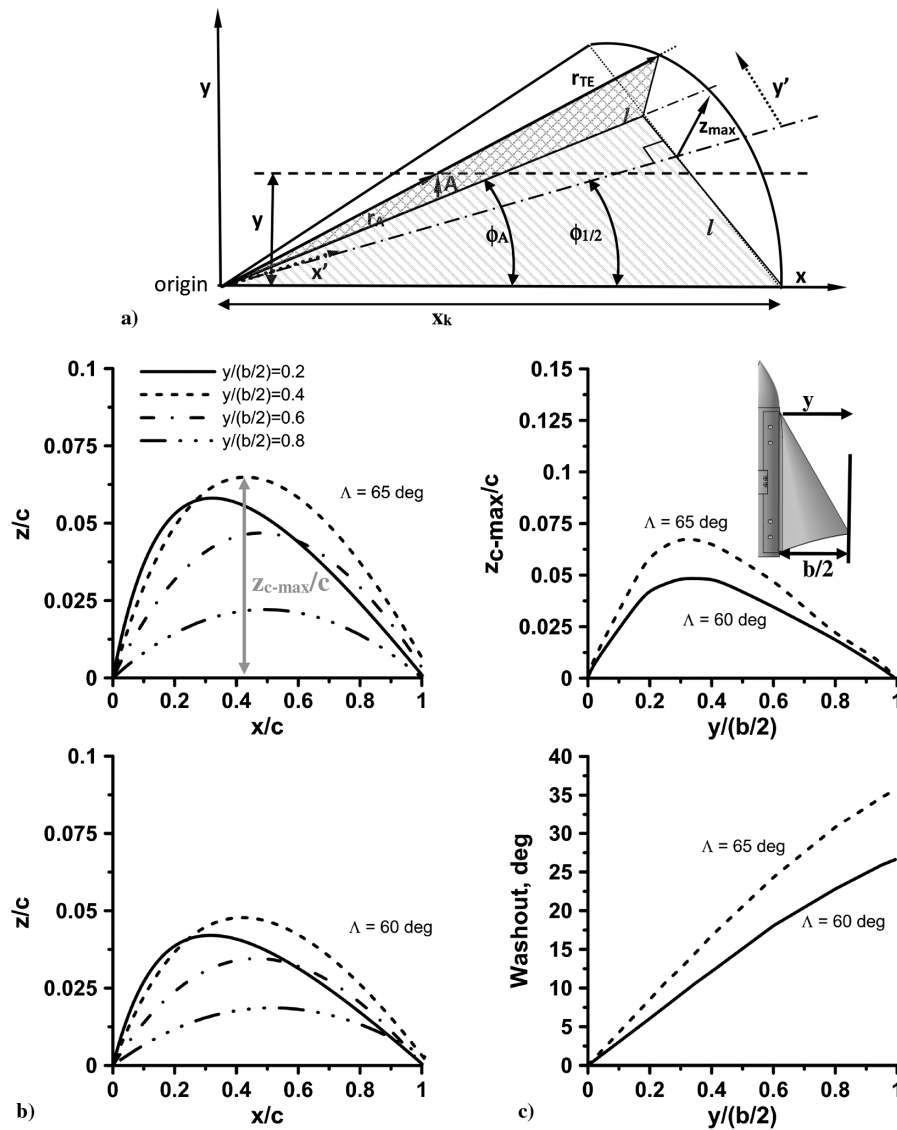


Fig. 2 Parabolic parawing a) geometry, b) airfoil sections, and c) spanwise maximum camber and geometric washout.

preliminary investigation, the wing shapes were rigid, rapid prototyped plastic, representing a fully inflated canopy. This form of testing alleviated issues with the physical construction of the model and has been used in other studies [13]; but, would not give insight into the canopy behavior at low angles of attack. In addition, for purposes of validation of numerical predictions, it is preferable to avoid uncertainty in the actual wing geometry that might be present if the model has a flexible skin.

Surface flow visualization was conducted using a surface paint consisting of titanium dioxide, linseed oil, kerosene, and oleic acid. Testing encompassed setting the model at the desired angle of attack, applying a thin film of the paint mixture to the surface, and rapidly bringing the wind tunnel to the test velocity. Both still and video images were recorded to aid in data interpretation.

III. Results and Discussion

A. Wing Geometry

Wing shapes formed from conical or parabolic cross sections are complicated, possessing significant geometric washout and spanwise variation of camber. In this experiment, the wing lobe is assumed to have a parabolic cross-sectional profile following Bass and Bertin, as this geometry is more representative for high slackness canopies than a conical cross-sectional geometry [12]. The shape of the trailing-edge section of the lobe is given by [12]

$$z_{TE}(y') = z_{\max} \left(1 - \left[\frac{y'}{l} \right]^2 \right) \quad (1)$$

The total projected trailing-edge length of each wing half is $2l$ (Fig. 2a). Sweeping the leading edge with resulting canopy inflation would see the trailing-edge length conserved. The trailing edge would then form into an assumed parabolic arc. To find the equation of the trailing-edge shape thus requires the determination of the peak canopy height z_{\max} . For the trailing edge, the arc length is given by

$$s_{\text{arc}} = 2 \int_0^l \sqrt{1 + \left(\frac{dz_{TE}}{dy'} \right)^2} dy' \quad (2)$$

Substitution of Eq. (1) into Eq. (2) and integrating yields

$$s_{\text{arc-para}} = l \sqrt{kl^2 + 1} + \frac{\sinh^{-1}(\sqrt{kl})}{\sqrt{k}} \quad (3)$$

where

$$k = 4z_{\max}^2/l^4 \quad \text{and}$$

$$l = x_k \sin(45 - \Lambda/2) \quad (\text{for the lobed wing, i.e., } \Lambda > \Lambda_0) \quad (4)$$

By definition, the total conserved trailing edge length for each lobe is given by

$$s_{TE} = 2x_k \sin(45 - \Lambda_0/2) \quad (5)$$

where $\Lambda_0 = 55$ deg for the current wing, and $x_k = 0.225$ m. Equating Eqs. (3) and (5) allows for the determination of the peak canopy height z_{\max} for any leading-edge sweep through its impact on l . Equation (1) then gives the canopy height along the trailing edge.

If the canopy is assumed to be conical in cross section, then the trailing edge is formed from a circular arc segment. In this case, the arc length of the trailing edge may be closely approximated as

$$s_{\text{arc-circ}} = \sqrt{(2x_k \sin(45 - \Lambda/2))^2 + (16/3)z_{\max}^2} \quad (6)$$

Equating Eqs. (5) and (6) allows calculation of z_{\max} . Comparison for the current test cases indicates z_{\max} values of 0.0407 and 0.0428 m (5% difference) using a circular arc or parabolic profile, respectively, for $\Lambda = 65$ deg. A sweep of 60 deg shows values of 0.0298 and

0.0307 m (3% difference) for the circular arc or parabolic profile, respectively. Consequently, for the current test cases, the lobe geometries will be similar using either a parabolic or circular arc section.

The streamwise sectional profile that results at a given y for the lobe may be estimated as follows: Note that this procedure is assumed to start from the keel ($y = 0$; see Fig. 2a) and not the fuselage centerline. For any specified y , the location of the section's leading edge is

$$x_{LE} = y/\tan(90 - \Lambda) \quad (7)$$

while the z coordinate of the leading edge is zero. At point A, the angle ϕ is given by

$$\phi_A = \tan^{-1}(y/x) \quad (8)$$

The angle to the centerline of each lobe is

$$\phi_{1/2} = 45 - \Lambda/2 \quad (9)$$

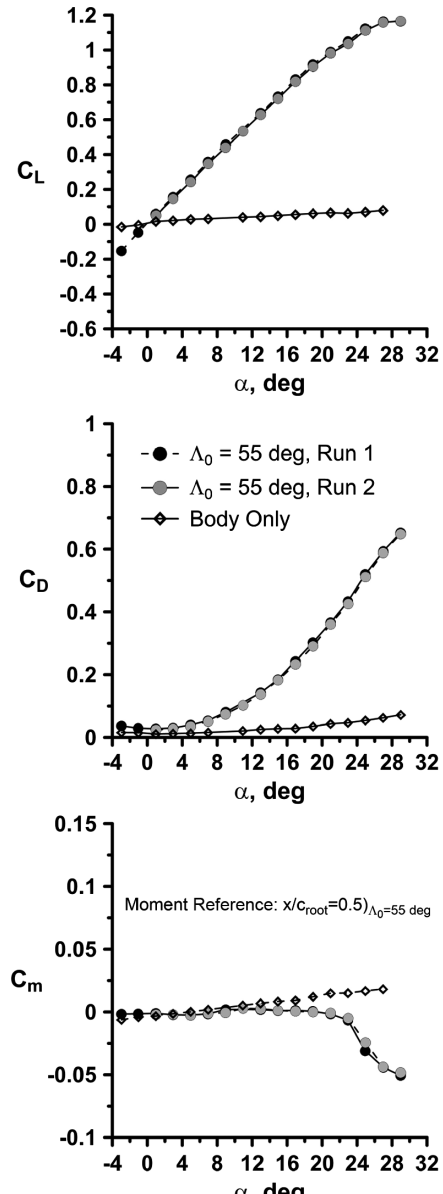


Fig. 3 Data repeatability and fuselage contribution.

while the magnitude of the vector from the origin to point A is

$$r_A = \sqrt{x^2 + y^2} \quad (10)$$

The trailing-edge location of the line passing through the origin and point A is

$$r_{TE} = \frac{x_k \cos(\phi_{1/2})}{\cos(\phi - \phi_{1/2})} \quad (11)$$

Then, the height (z value) of point A is

$$z_A = (r_A/r_{TE})z_{TE}(y') \quad (12)$$

where

$$y_{TE}' = x_k \sin(\phi_{1/2} - \phi) \quad \text{and} \quad y' = y_{TE}' \quad (13)$$

To generate a streamwise airfoil profile, a value of y is selected and x is then varied from the leading edge to the trailing edge while evaluating Eqs. (8–13). Note that the methodology presented above is only applicable to NASA-type parawings where the leading edge and keel length are equal, and is thus consistent with the current test models. As an example of application, this procedure yields the lobe geometric data shown in Figs. 2b and 2c. For the purpose of examining wing geometry, $b/2$ is defined as the span of the wing half extending from the fuselage (such that the root chord becomes the keel length x_k). The airfoil camber line is shown in Fig. 2b for spanwise locations of 0.2, 0.4, 0.6, and 0.8 of the semispan measured from the keel. Extraction of the maximum airfoil camber at each spanwise location as a fraction of the local chord as well as the wing's washout are presented in Fig. 2c. The wing profile is seen to be heavily cambered, with the maximum camber occurring between 30 to 45% of the span (Fig. 2c). At a spanwise station, the peak camber is further forward inboard and moves aft outboard, approaching a circular arc profile (Fig. 2b). As may be expected, increasing wing sweep increases $z_{c-\max}/c$. Washout (or twist) is very high, especially

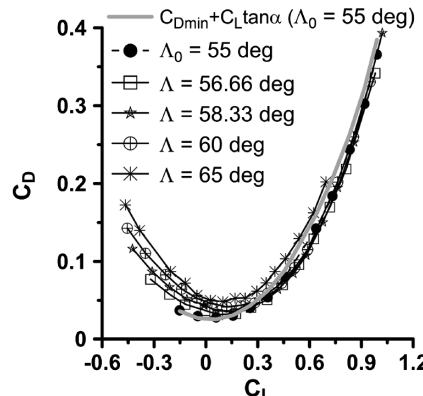
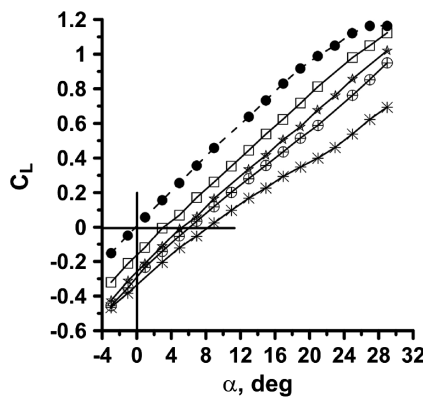


Fig. 4 Effect of leading-edge sweep on longitudinal force coefficients.

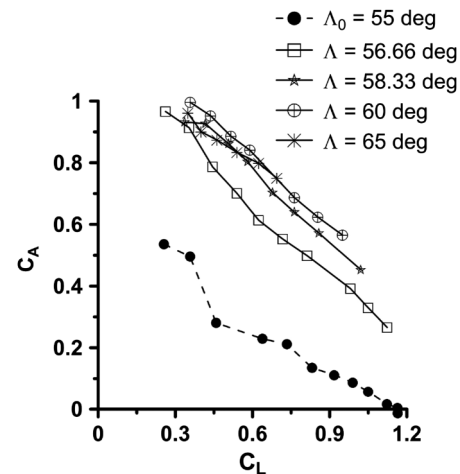


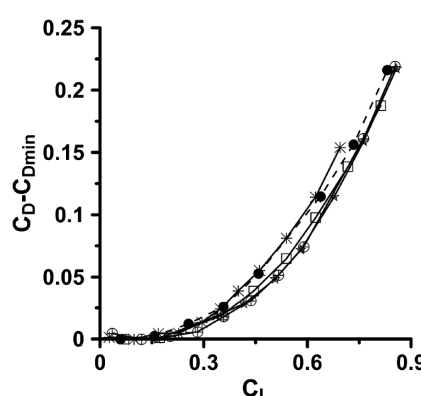
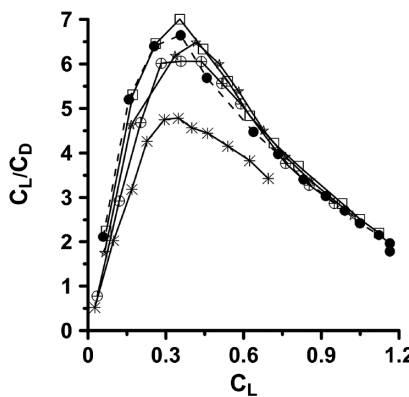
Fig. 5 Effect of leading-edge sweep on attainable axial force coefficient.

as the tips are approached and will serve to unload the wingtip regions and shift loading inboard at low to moderate angles of attack.

B. Symmetrical Data

Figure 3 shows data repeatability as well as the contribution of the fuselage to the loads. Data repeatability is seen to be excellent. The effect of the fuselage was examined by using clamshells that completed the cylindrical shape of the body but had no wings attached. Although this form of testing does not indicate the effect of the wings on the body, or the body on the wings, it does give an estimate of the fuselage influence. The fuselage contribution is seen to be moderate for both lift and drag but adds a noseup pitching moment reflective of concentrated loading close to the nose.

The lift coefficient is seen to attenuate significantly with increasing Λ (Fig. 4), constituted of both a reduction in lift curve slope and a positive shift in the zero-lift angle of attack. Within the limitation of the balance's maximum allowable angle of attack (i.e., 30 deg), sweep is seen to delay stall, as documented in other studies [11,20]. Sweep is



also seen to be deleterious to C_D , increasing the minimum drag coefficient. For reference, the drag coefficient assuming zero leading-edge suction (i.e., $C_D = C_{D\min} + C_L \tan \alpha$) is also presented, based on $C_{D\min}$ for the $\Lambda_0 = 55$ deg wing. The experimentally measured drag coefficient of the planar wing ($\Lambda_0 = 55$ deg) is observed to fall below this line, indicating that the circular profile of the leading edge is able to generate some leading-edge suction. To gauge the effect of sweep on drag due to lift, the drag less the minimum drag coefficient ($C_D - C_{D\min}$) is also presented. For all cases excluding $\Lambda = 65$ deg, sweep reduces drag due to lift, which is most pronounced for the $\Lambda = 58.33$ and 60 deg case. The geometry of the surface yields a forward acting normal force component at moderate to high angles of attack that will oppose drag. Sweep has a moderate impact on the aerodynamic efficiency (C_L/C_D) unless the slackness is large ($\Lambda = 65$ deg). Thus, the increase in $C_{D\min}$ is compensated by the reduction in drag due to lift. It follows that the range of the flight vehicle will not be markedly influenced by moderate increases in leading-edge sweep greater than Λ_0 .

The attainable (i.e., the actual axial force divided by the theoretical maximum) axial force coefficient [Eq. (14)] is plotted in Fig. 5 and gives insight into the forward-orientated chordwise force:

$$C_A = \frac{C_L \sin(\alpha) - (C_D - C_{D\min}) \cos(\alpha)}{C_L \sin(\alpha) - (C_L^2 / (\pi AR)) \cos(\alpha)} \quad (14)$$

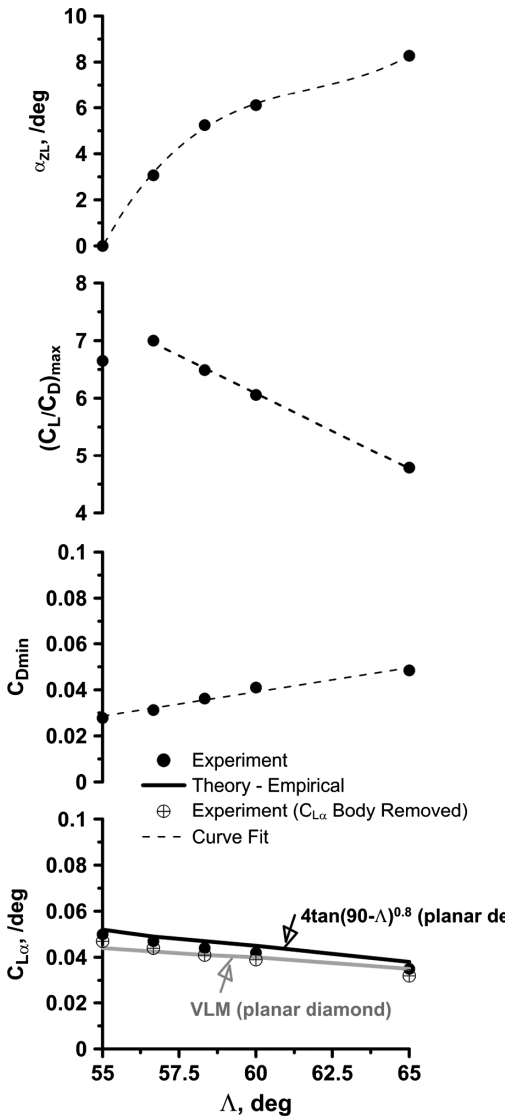


Fig. 6 Key performance characteristics as affected by leading-edge sweep.

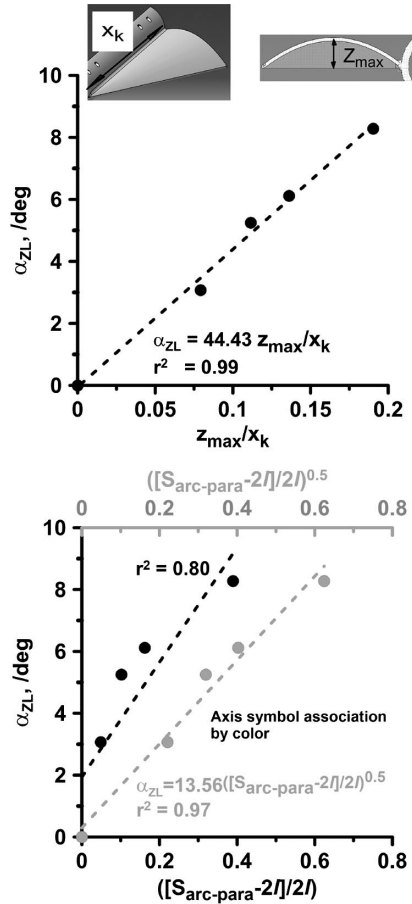


Fig. 7 Correlation of measured α_{ZL} with a) peak lobe height and b) slackness parameter.

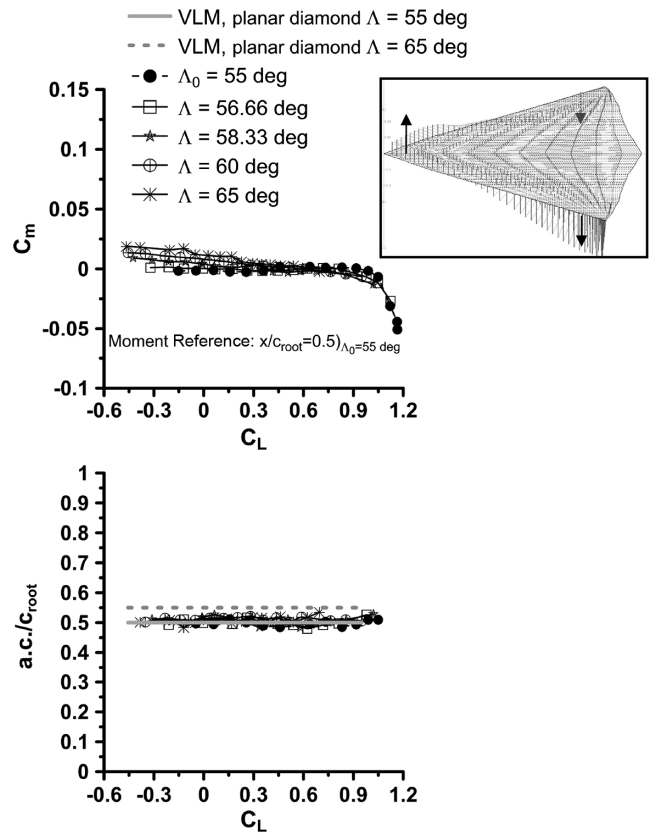


Fig. 8 Effect of leading-edge sweep on C_m and calculated aerodynamic center (a.c.) location; inset shows AVL simulation of load distribution over the $\Lambda = 60$ deg parawing ($C_L = 0$).

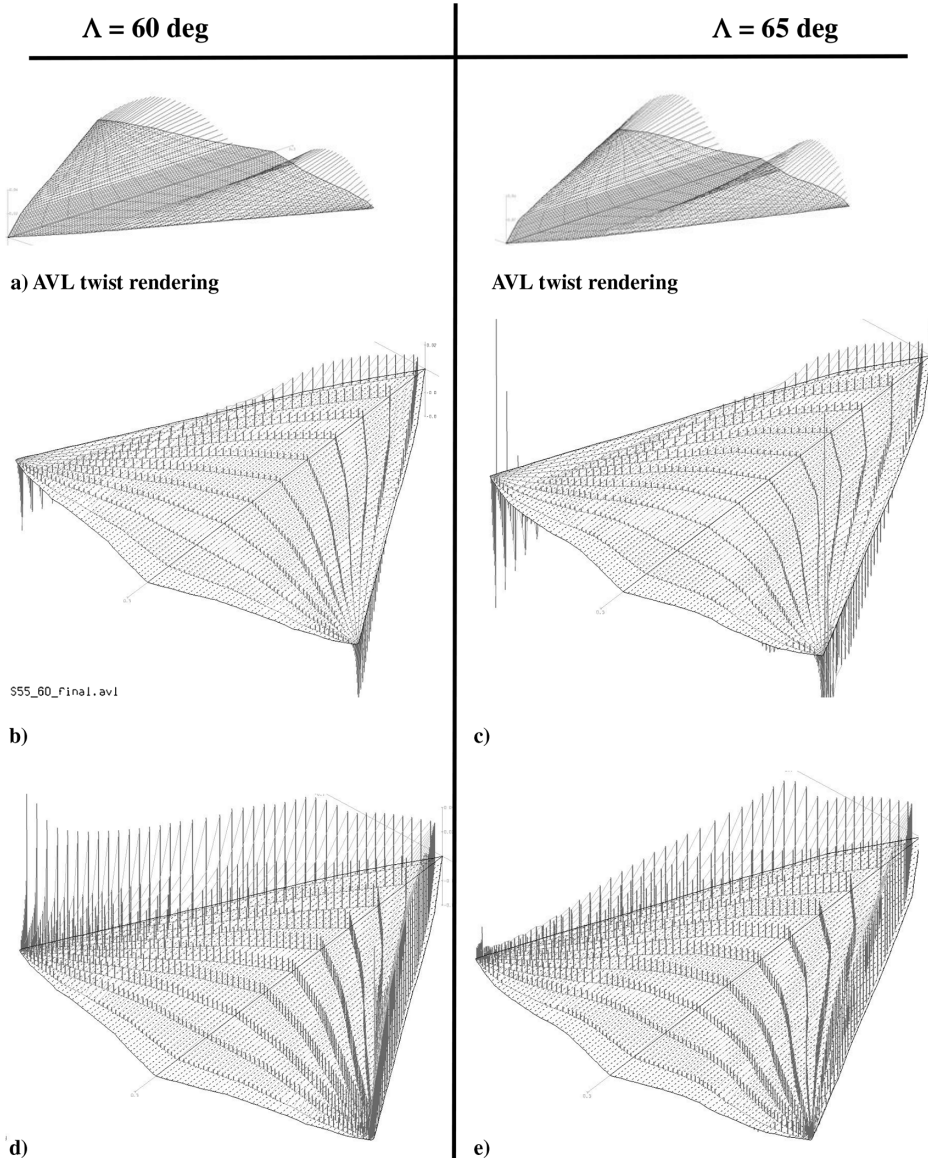


Fig. 9 AVL rendering of a) geometric twist and surface loading (nondimensional bound vortex strength) for α equal to b) 10 deg, c) 10 deg, d) 20 deg, and e) 20 deg.

Equation (14) represents the ratio of the experimentally measured axial force divided by the theoretical maximum axial force assuming full leading-edge (elliptic spanwise loading) suction. Thus, its bounds range from zero to one. The axial force is seen to reduce with C_L , which is an effect commonly associated with leading-edge separation. The axial force for all lobed configurations is significantly higher than compared to the planar wing. The reduction in performance of the $\Lambda = 65$ deg wing noted in Fig. 4 follows from its large $C_{D\min}$ penalty, even though it develops significant axial thrust.

A summary of key aerodynamic parameters is displayed in Fig. 6. The zero-lift angle of attack is seen to rapidly shift positive with initial sweep but then flatten out. The peak lift-to-drag ratio is seen to increase slightly for a 1.66 deg increase in sweep ($\Lambda = 56.66$ deg) over the planar wing ($\Lambda_0 = 55$ deg) and then decrease fairly linearly for the data range presented. Similarly, the minimum drag coefficient also increases linearly with wing sweep. The lift curve slope was extracted from the experimental data and is presented in conjunction with an analytic estimate for a delta wing and a vortex lattice model (VLM)[‡] estimate for the wing. These estimates are included to see whether a simplified approximate method (that is easier and more

rapidly implemented) may be used to compute the lift curve slope of the parawings. The VLM estimate is simplified in the sense that the geometry is that of the projected parawing yielding a diamond wing; thus, the numerically simulated wing is a flat plate. AVL (Athena vortex lattice) was used for this analysis with 400 panels (distributed 10 chordwise by 40 spanwise). The analytic estimate for the delta wing is given by [21]

$$C_{L\alpha} = 4 \tan(90 - \Lambda)^{0.8} \quad (15)$$

and is seen to show reasonable agreement with experiment, as does the VLM (i.e., AVL) estimate. It would be expected that the agreement of Eq. (15) with experiment would deteriorate as Λ_0 gets smaller (i.e., the geometry becomes a more pronounced diamond wing in planform). The lift curve slope of the fuselage was estimated using the data in Fig. 3, and was subsequently removed from that recorded for the whole model (yielding the crossed circle symbol seen in Fig. 6). Agreement between this experimental measurement and the VLM estimate for the projected diamond wing is excellent, and suggests a simple approach for estimating the lift curve slope of this type of geometry. The agreement shown in Fig. 6 also implies that the projected planform geometry is responsible for $C_{L\alpha}$, while camber and washout define α_{ZL} .

[‡]Data available online at [http://web.mit.edu/drela/Public/web\(avl](http://web.mit.edu/drela/Public/web(avl) [retrieved 10 January 2017].

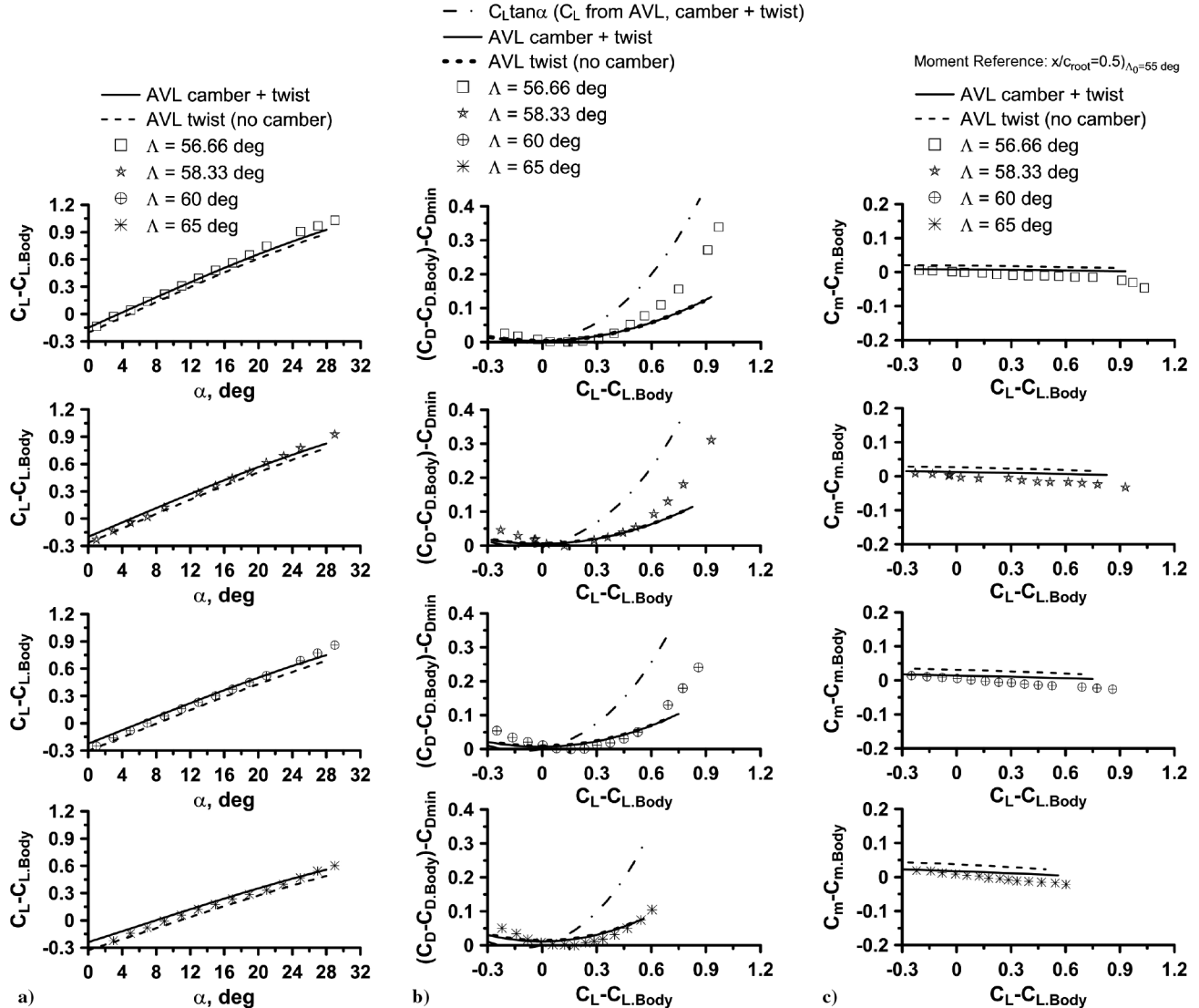


Fig. 10 Comparison of experiment and AVL simulation for a) lift, b) drag, and c) pitching moment coefficients.

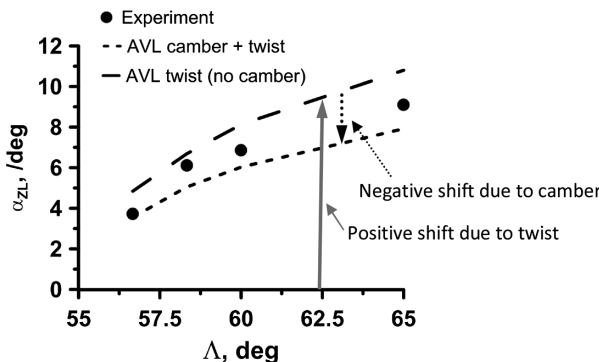


Fig. 11 Comparison of experiment and AVL α_{ZL} predictions.

As noted, the zero-lift angle of attack variation with Λ is nonlinear (Fig. 6). Correlating this parameter with the wing geometry would be useful to understanding its behavior. It would follow that α_{ZL} should have some dependency on the peak lobe height. Plotting α_{ZL} as a function of the normalization of z_{\max} by the keel length x_k yields Fig. 7a. A linear dependency is evident, such that the zero-lift angle of attack shift with increasing slackness is directly proportional to the increase in the peak lobe height (i.e., $\alpha_{ZL} = 44.43 z_{\max}/x_k$). The slackness parameter [16]

$$S_p = (S_{arc-para} - 2l)/(2l) \quad (16)$$

is also examined as a correlating parameter, as presented in Fig. 7b. Correlation is poor as shown, but improves significantly if the square root of the slackness parameter is used (although it is still slightly inferior to that based on peak lobe height).

The effect of leading-edge sweep on the measured pitching moment and calculated aerodynamic center is shown in Fig. 8. The most visible effect is at low C_L , where greater leading-edge sweep causes an increasingly positive pitching moment. This behavior stems from the high washout inherent in parawings. At low C_L , the inboard wing section will generate positive lift, while the outboard sections, due to the extreme washout, will produce negative lift. Consequently, lift inboard will act further forward than that outboard (as implied by consideration of the geometry, the outboard sections are aft), yielding a noseup pitching moment; see inset sketch from a vortex lattice simulation, as will be documented subsequently. The location of the aerodynamic center is weakly affected by sweep with a value of approximately 50% of the root chord. VLM estimation assuming a planar diamond wing projection with $\Lambda = 55$ and 65 deg is seen to bound the experimental data but suggests a greater dependence on sweep than that seen in the experimental results.

C. Numerical Simulation

The parawing geometries were simulated using AVL, accounting for the camber and twist of the wings, which were determined using

Eqs. (7–13). Forty spanwise panels were used in conjunction with ten chordwise. Variation in the paneling density (doubling and halving the number of spanwise panels) showed little impact on the predictions. Figure 9a shows example paneling as well as the AVL implementation of the geometric twist. The wings were numerically modeled by simulating the lobes as extending from the keel, while the area located under the fuselage was assumed to be planar.

Renderings of surface loading (the local lift coefficient) for the $\Lambda = 60$ and 65 deg wings at 10 and 20 deg angles of attack are shown in Figs. 9b–9e and are representative of the trends associated with all configurations. At a moderate angle of attack ($\alpha = 10$ deg), twist results in negative lift in the vicinity of the wingtips, with increasing Λ causing this downforce to extend further inboard. A byproduct of this loading distribution is an increase in the noseup pitching moment as observed in Fig. 8. In addition, negative lift will cause a significant drag increase (as the normal force will be acting on the windward face of the lobe); but, realistically, it would precipitate collapse of the canopy. Increasing the angle of attack shows the development of positive lift in the wingtip regions, although greater sweep attenuates the magnitude. It may also be inferred that the angle of attack at which the outboard loading changes from negative local lift to positive increases with canopy slackness. Notice that loading is heavily

concentrated along the leading edges, stemming from AVL's inviscid formulation; the leading-edge loading tends toward a singularity as predicted by slender wing theory.

Comparisons of experiment with AVL simulations are shown in Figs. 10a–10c. Also included are additional simulations where the airfoil profile was assumed to be a flat plate; thus, the aerodynamic effects are due to angle of attack and twist only. This allows the effect of camber to be examined directly as the difference between the "camber + twist" and "no camber" predictions. In all comparisons, the effect of the fuselage is removed using the data in Fig. 3. Lift prediction (Fig. 10a) is seen to be very good and shows close agreement with experiment for all geometries. Camber is seen to add a constant lift increment that increases moderately with Λ due to the greater magnitude of the camber; see Figs. 2b and 2c. The agreement shown between experiment and numerical simulation suggests that viscous effects are negligible as AVL is an inviscid formulation. Consequently, effects due to separation that may include leading-edge vortex formation (as will be discussed subsequently) would not appear to impact the results.

Predictions of the drag coefficient appear somewhat less satisfactory; see Fig. 10b. The estimate of the lift-dependent drag is seen to improve with sweep. Also included in Fig. 10b is the drag that

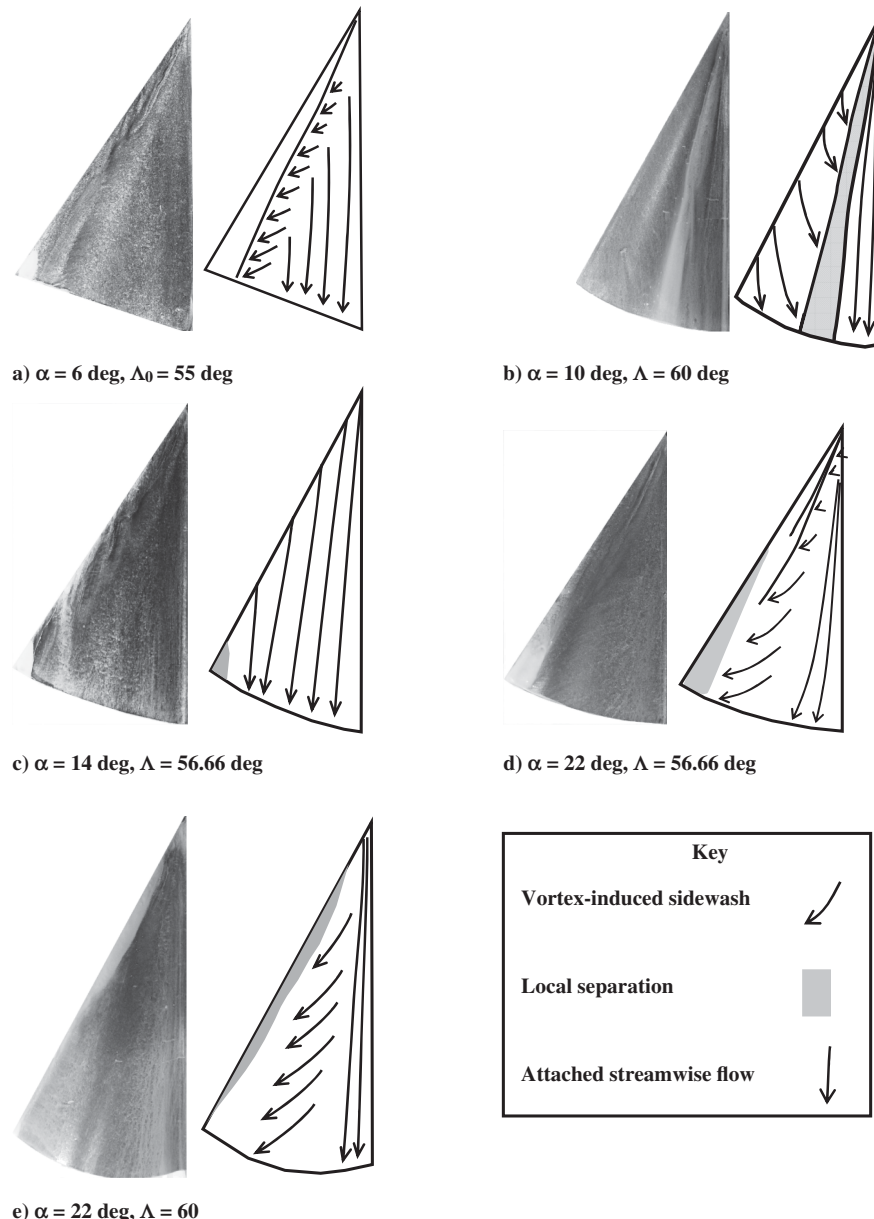


Fig. 12 Example skin-friction patterns over the a) planar wings and b)–e) parawings.

would result if the wing was planar and sharp edged and may be viewed as an upper drag bound (i.e., $C_L \tan \alpha$). The AVL simulations do not account for any loss of leading-edge suction due to flow separation along the leading edge. Consequently, it may be expected that increasing Λ , which would serve to suppress leading-edge separation to higher α , should give better agreement with AVL estimates at higher lift coefficients, as seen in Fig. 10b. Also evident is that camber does not contribute to the drag coefficient (lines for camber + twist and no camber are coincident).

Estimates of the pitching moment coefficient show good agreement with experiment (Fig. 10c) in terms of magnitude and slope. Camber contributes a fairly significant nosedown pitching moment (observed as the difference between the solid and dashed lines) that increases with wing leading-edge sweep. Twist is seen to contribute a moderate noseup pitching moment (indicated by an upward shift in the moment curve with increasing Λ). Calculation of

the location of the aerodynamic center from the AVL simulations indicates a value ranging from 51 to 52% of the root chord, closely matching the results in Fig. 8.

The ability of AVL to predict the parawing's zero-lift angle of attack is explored directly in Fig. 11, where estimates with and without camber inclusion are compared with experimental measurement. The numerical estimates are generally in good agreement with experiment. The effects of twist and camber are seen to oppose each other. Twist, which dominates, shifts the zero-lift angle of attack in the positive α direction due to attenuated loading, while the camber contribution serves to lessen the positive α_{ZL} shift (due to augmented loading for a given α).

D. Flow Visualization

Surface flow patterns are presented in Fig. 12 as rendered using titanium dioxide. Additionally, orientation of the skin-friction lines

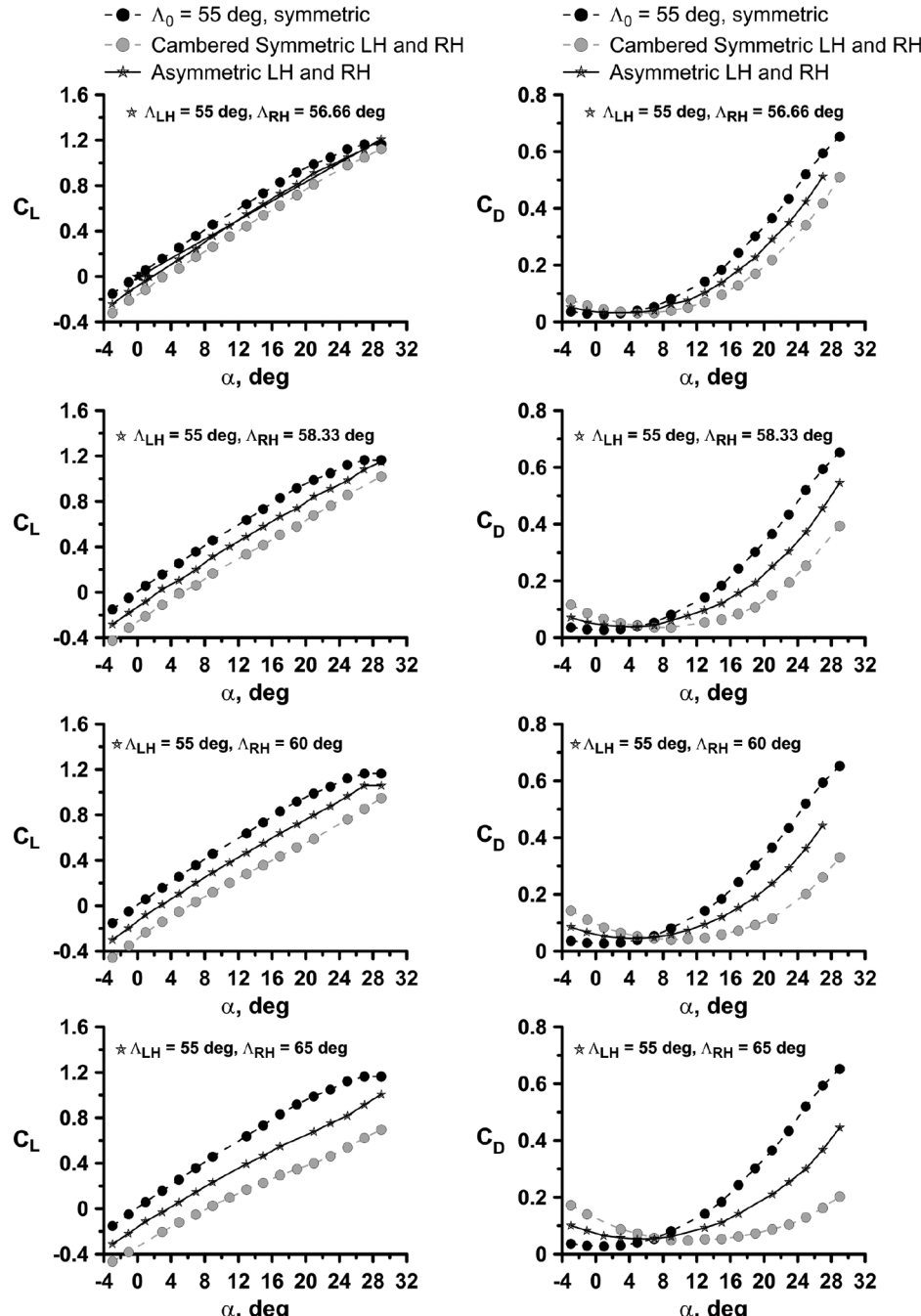


Fig. 13 Measured effect of asymmetric sweep on a) lift and b) drag coefficients.

as observed from video is also presented. As the flow patterns vary consistently with angle of attack, select images are presented that summarize the main features. The planar delta (Fig. 12a) shows a typical pattern that may be expected for a moderate sweep delta; leading-edge separation resulting in the formation of a conical vortex above the wing causing sidewash. A secondary separation line is also present. Greater angle of attack shows an increase in the size of the vortex-induced sidewash with a concomitant lessening of the orientation of the sidewash lines, suggestive of a weakening vortex and greater vortex-wing proximity. Sweeping the leading edge to form the parawing has the net effect of suppressing leading-edge separation at moderate angles of attack such that the flow over the leeward wing surface is primarily streamwise and attached (Figs. 12b and 12c). However, greater Λ causes flow propagating from the leading edge to have a moderate inward orientation (caused by the strong spanwise load gradients caused by the washout). Confluence of these limiting streamlines with those deflected spanwise by the fuselage leads to a region of separation as seen in Fig. 12b. Increasing α shows the appearance of leading-edge separation on the cambered profiles (Figs. 12c and 12d). The separation manifests in the form of localized fluid deposits originating from the wingtip and extending toward the apex with an increasing angle of attack. Also evident further inboard is spanwise-orientated crossflow suggestive of the presence of a leading-edge vortex; see Figs. 12d and 12e. Increasing Λ delayed the α at which these crossflow surface traces become visible. Note that some of the skin-friction patterns identified in Fig. 12 may not be clear in the still images but were obvious in recorded video.

It may be expected that the extreme washout inherent in the more highly swept parawings would suppress leading-edge separation. Geometrically, the angle of attack normal to the leading edge may be calculated using

$$\alpha_n = \tan^{-1}(\tan(\alpha) / \cos(\Lambda)) \quad (17)$$

As an example, evaluation of Eq. (17) shows that α_n approaches 39 deg for $\Lambda = 60$ deg and $\alpha = 22$ deg, comfortably exceeding the washout seen in Fig. 2c. Consequently, despite the significant washout, localized leading-edge separation is still present, especially toward the wingtips.

E. Asymmetric Data

The functionality of asymmetric wing sweep as a means of achieving lateral control is examined in Figs. 13 and 14. Moment coefficients are in body axes unless stated otherwise. Asymmetry is implemented by using the planar left-hand 55 deg swept-wing panel and systematically increasing the sweep of the right-hand panel. Results for the measured lift and drag coefficient are presented in Figs. 13a and 13b. Also included are data for the symmetric planar wing and the symmetric parawing cases. These two cases form the upper and lower bounds for the coefficient. The lift coefficient for the asymmetric model is seen to fall midway between the $\Lambda_0 = 55$ deg and symmetric parawing cases. The results imply that the left- and right-hand side wing panels function essentially independently. The drag coefficient data, presented as a function of α , display a crossover for an angle of attack less than about 8 deg. For a given angle of attack above 8 deg, the parawing produces less drag than the planar wing (due to the loss of lift). The implication is a significant differential drag coefficient between the wing halves, with the potential complication that the drag switchover would affect the sign of the imposed yawing moment.

Lateral directional performance characteristics are summarized in Fig. 14. Asymmetry produces a marked rolling moment coefficient, with a dependency on angle of attack that increases with canopy slackness. Increasing slackness (i.e., increasing the sweep) of the right-hand side wing yields a corresponding increase in C_l . The sign of the moment is reflective of the greater lift production by the left-hand side planar wing panel. The accompanying yawing moment coefficient shows a sign reversal around 8 deg angle of attack. In addition, side force also shows a sign change at this α . The yawing

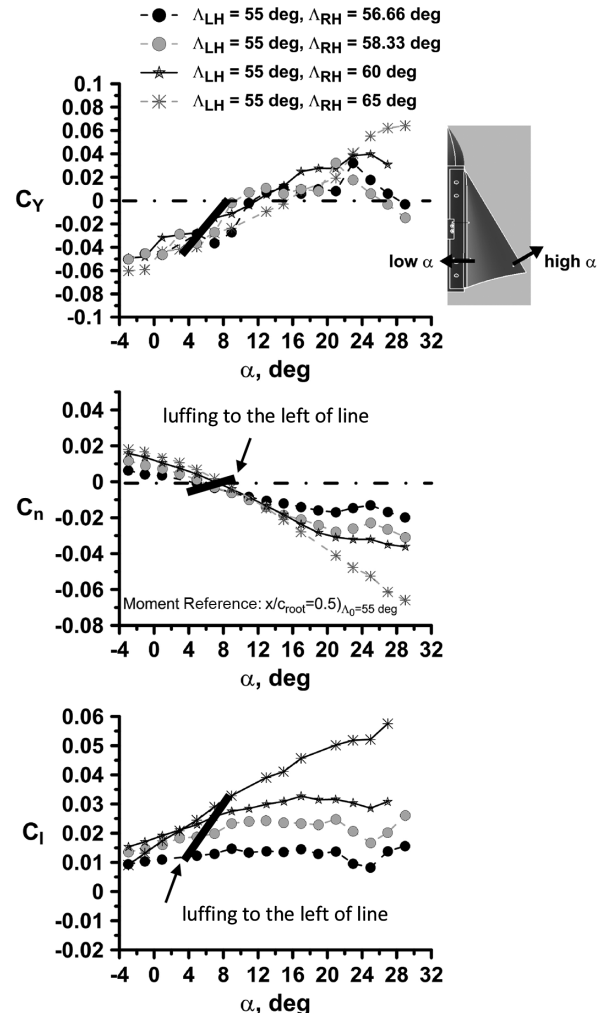


Fig. 14 Effect of asymmetric sweep on lateral/directional performance parameters (body axes).

moment sign switch corresponds to the angle-of-attack range at which the left/right wing panel drag differential switches; see Fig. 13. The drag differential and side force are related. At low α , the resultant positive lift force on the right-hand side parawing panel acts inboard of the peak lobe height, while the outboard regions of the right-hand wing experience a negative lift that acts on the windward surfaces (Figs. 9b and 9c), with both loads giving a negative side force and no forward acting axial force to oppose drag. At high angles of attack, the resultant force acts outboard of the peak lobe height so by causing positive side force and contributing to a reduction in drag; see the inset sketch in Fig. 14. As discussed by Bass and Bertin [12], the angle of attack has a notable influence on the location of the center of pressure of the parawing. At low angles of attack, the center of pressure is close to the keel (due to the twist attenuating outboard loading significantly), but moves closer to the wingtip at higher α as the wingtip regions load up.

Note that Fig. 14 shows the full tested α range (for completeness) and is representative for a rigid parawing. However, for a flexible skinned wing, luffing (indicated by a flapping and rippling skin or, more specifically, when the leading-edge suction tends to zero and the local lift is due to camber effects [16]) typically occurs at low to moderate angles of attack. Experimental data [11] only shows results for lift coefficient values of approximately 0.2 and greater, as canopy inflation below these C_L values was inconsistent. Consequently, as a conservative bound, the measured α_{ZL} may be used as a luffing boundary. These boundaries are included in Fig. 14 and suggest that sign reversals in the coefficients will not occur with a flexible canopy for any practical flight angles of attack.

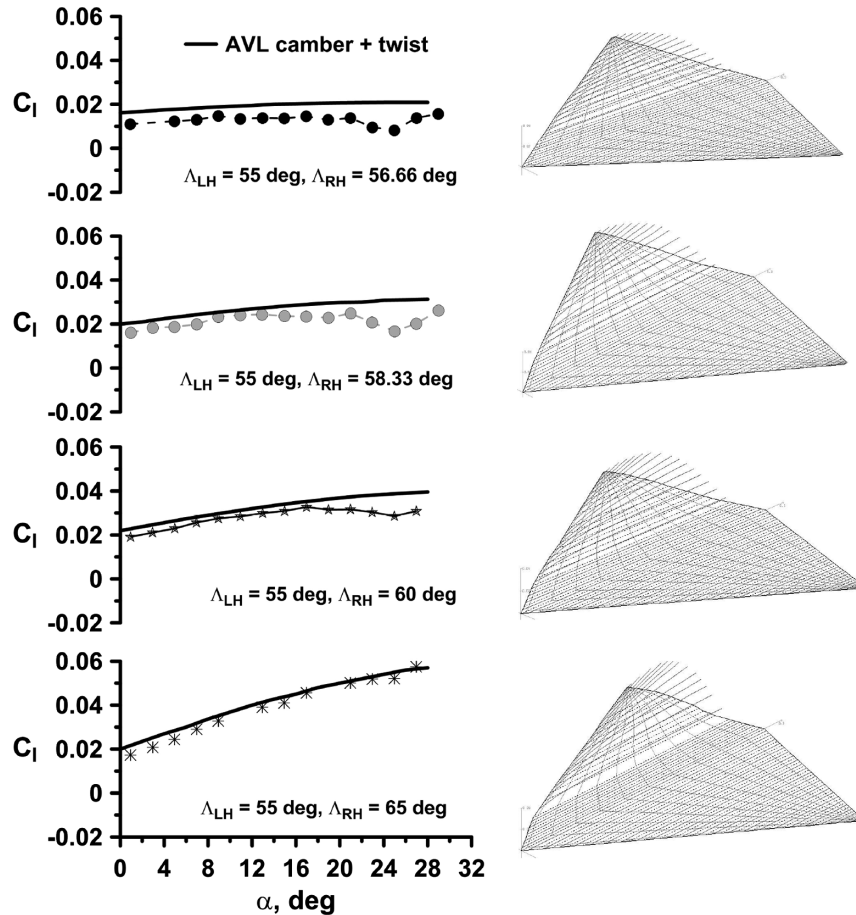


Fig. 15 Comparison of experiment and AVL predicted rolling moment coefficients (body axes).

AVL was also examined to determine if the formulation could simulate asymmetric wing sweep. The experimental geometry was simulated as shown in the surface panel and twist renderings shown in Fig. 15. Agreement with experiment is seen to be very good in terms of both magnitude and angle-of-attack dependence. Consequently, it might be inferred that the rolling moment behavior is essentially inviscid in nature, and that the separation behavior shown in the surface flow visualization of Fig. 12 has a secondary effect on net loading. It would not be expected that AVL could capture the physics associated with the generation of the yawing moment, noting C_n 's strong dependence on differential wing drag, which required simulation of viscous effects (primarily in terms of loss of leading-edge suction on the planar wing panel).

The effectiveness of asymmetric wing sweep is examined in Fig. 16, where results are compared with those from [22] for a similar aspect ratio ($AR = 3.13$) rectangular wing (NACA 64A010 section) with 25% chord ailerons. The moments are in a wind axes reference frame to be consistent with the data in [22]. Results are presented for an aileron of 24 and 48% of the wing span and aileron angles of 10 and 20 deg. Note that the current experimental parawing data are the same in Figs. 16a–16d; the aileron data vary such that Figs. 16a and 16b show results for a 24% span aileron as affected by α . Similarly, Figs. 16c and 16d show the impact of α on a 48% span aileron.

Increasing the sweep of the right-hand side wing is seen to generate a positive rolling moment, a result of lift loss on this wing panel as compared to the left wing (Fig. 16). The increase in rolling moment with Δ_{RH} is not linear, with increasing sweep yielding a proportionally smaller moment increment. Unlike an aileron, the rolling moment is moderately dependent on angle of attack, which may be a less than desirable attribute. The magnitude of the induced moments is comparable to those generated by an aileron, suggesting that differential wing sweep may be viable for roll control but may require greater complexity in the flight controller. The adverse

yawing moment is greater in magnitude than that of an aileron for an equivalent rolling moment. The resulting yawing moments are also concerning, in that a moment reversal dependent on angle of attack is present. This behavior stems directly from the differential drag as seen in Fig. 13b. However, the results may be a bit misleading. The tested parawings are rigid, and thus fully inflated. A flexible skin generally results in canopy collapse or luffing at low angles of attack, which are typically greater than the measured α_{ZL} . Consequently, the yawing moment reversal may be less relevant than indicated as it resides in a α range in which the UAV will not operate. Thus, the results for $\alpha = 0$ and 6 deg are representative of a rigid test model but not necessarily a flexible skinned flight vehicle.

IV. Conclusions

A low-speed wind-tunnel investigation is presented, characterizing the effect of both symmetric and asymmetric sweep on a dual-lobe canopy parawing geometry. Numerical simulations using a vortex lattice method are also detailed. Increasing the slackness of the canopy (by varying the leading-edge sweep) shifted the zero-lift angle of attack in the positive direction and simultaneously reduced the lift curve slope. The positive shift is caused by significant washout and is opposed by camber that results as the slackness of the wing's lobe increases. The minimum drag coefficient and maximum lift-to-drag ratio both showed a linear dependence on the wing's leading-edge sweep angle. Numerical simulations showed close accord with experiment for both the lift and pitching moment coefficients. Accord with experiment for the drag coefficient improved with increasing canopy slackness. Wing asymmetry, achieved using a planar left-hand wing panel and a lobed right-hand panel, showed the generation of rolling moments of comparable magnitude to that of an aileron. Numerical simulation showed good agreement with the experimentally measured rolling moment coefficients. The induced rolling moments indicated an increasing dependence on angle of attack as

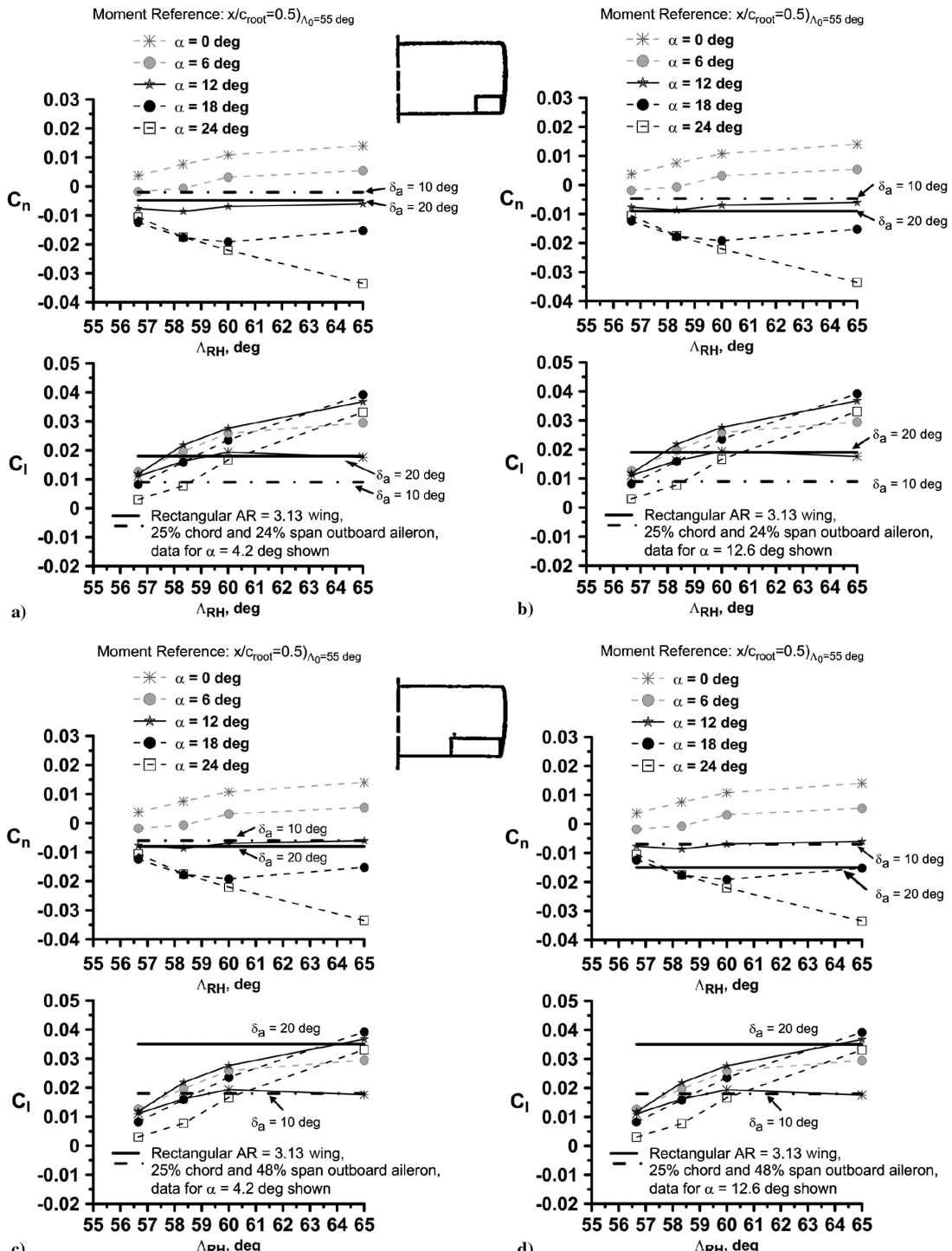


Fig. 16 Comparison of parawing roll and yaw moments with a rectangular wing: a)–b) 24% span aileron and c)–d) 48% span aileron. Inset sketches show the aileron location on the wing.

the lobe slackness increased. Future research will encompass implementation of a servoactuated wing leading edge in conjunction with a canopy formed using a flexible skin. The preliminary results suggest that a variable sweep parawing geometry may present as a viable planform for a small unmanned aerial vehicle in terms of stall resistance and achievable lateral control.

Acknowledgment

The authors would like to acknowledge support for Sho Okayama provided by an Embry-Riddle Aeronautical University Ignite research grant.

References

- [1] Gomez, J. C., and Garcia, E., "Morphing Unmanned Aerial Vehicles," *Smart Materials and Structures*, Vol. 20, No. 10, 2011, Paper 103001. doi:10.1088/0964-1726/20/10/103001
- [2] Jacob, J. D., and Smith, S., "Design of HALE Aircraft Using Inflatable Wings," *46th AIAA Aerospace Science Meeting and Exhibit*, AIAA Paper 2008-0167, Jan. 2008. doi:10.2514/6.2008-167
- [3] Weisshaar, T., "Morphing Aircraft Technology—New Shapes for Aircraft Design," *Multifunctional Structures/Integration of Sensors and Antennas*, Rept. RTO-MP-AVT-141, Neuilly-sur-Seine, France, Oct. 2006.
- [4] Armando, R. R., "Morphing Aircraft Technology Survey," *45th AIAA Aerospace Sciences Meeting and Exhibit*, AIAA Paper 2007-1258,

- Jan. 2007.
doi:10.2514/6.2007-1258
- [5] Skillin, M., and Crossley, W., "Modeling and Optimization for Morphing Wing Concept Generation," NASA CR-2007-214860, March 2007.
- [6] Brown, G., Haggard, R., and Norton, B., "Inflatable Structures for Deployable Wings," *AIAA Aerodynamic Decelerator Systems Technology Conference and Seminar*, AIAA Paper 2001-2068, May 2001.
doi:10.2514/6.2001-2068
- [7] Jacob, J. D., and Smith, S. W., "Design Limitations of Deployable Wings for Small Low Altitude UAVs," *47th AIAA Aerospace Sciences Meeting*, AIAA Paper 2009-0745, 2009.
doi:10.2514/6.2009-745
- [8] Rogallo, G. S., and Rogallo, F. M., "Flexible Kite," U.S. Patent Office No. 2,546078, March 1951.
- [9] Rogallo, F. M., Lowry, J. G., Croon, D. R., and Taylor, R. T., "Preliminary Investigation of a Paraglider," NASA TN D-443, 1960.
- [10] Barte, G. R., "Flexible Wings for Maneuvering and Landing Application in the De-Coupled Concept," AIAA Paper 1967-0200, Jan. 1967.
doi:10.2514/6.1967-200
- [11] Naeseth, R. L., and Gainer, T. G., "Low-Speed Investigation of the Effects of Wing Sweep on the Aerodynamic Characteristics of Parawings Having Equal-Length Leading Edges and Keel," NASA TN D-1957, 1963.
- [12] Bass, R. L., III, and Bertin, J. J., "Theoretical Investigation of the Lift and Drag Characteristics of Flexible Parawings at Subsonic Speeds," *Journal of Aircraft*, Vol. 7, No. 2, 1970, pp. 130–137.
doi:10.2514/3.44135
- [13] Fournier, P. G., and Bell, B. A., "Low Subsonic Pressure Distributions on Three Rigid Wings Simulating Paragliders with Varied Canopy Curvature and Leading-Edge Sweep," NASA TN D-983, 1961.
- [14] Nielsen, J. N., and Burnell, J. A., "Theoretical Aerodynamics of Flexible Wings at Low Speeds, V—Engineering Method for Estimating Parawing Performance," Kept. 209, Vidy, Dec. 1965.
- [15] Mendenhall, M. R., Spangler, S. B., and Nielsen, J. N., "Review of Methods for Predicting the Aerodynamic Characteristics of Parawings," AIAA Paper 1968-0010, 1968.
doi:10.2514/6.1968-10
- [16] Mendenhall, M. R., Spangler, S. B., and Nielson, J. N., "Investigation of Methods for Predicting the Aerodynamic Characteristics of Two Lobed Parawings," NASA CR 1166, Sept. 1968.
- [17] Pankhurst, R. C., "A Method for the Rapid Evaluation of Glauert's Expressions for the Angle of Zero Lift and the Moment at Zero Lift," R&M No. 1914, British A.R.C., London, 1944.
- [18] Weissinger, J., "The Lift Distribution of Swept-Back Wings," NACA TM 1120, 1947.
- [19] Diederich, F. W., and Zlotnick, M., "Calculated Spanwise Lift Distributions and Aerodynamic Influence Coefficients for Swept Wings in Subsonic Flow," NACA TN 3476, 1955.
- [20] Polhamus, E. C., and Naeseth, R. L., "Experimental and Theoretical Studies of the Effects of Camber and Twist on the Aerodynamic Characteristics of Parawings Having Nominal Aspect Ratios of 3 and 6," NASA TN D-972, Jan. 1963.
- [21] Traub, L. W., "Prediction of Delta Wing Leading-Edge Vortex Circulation and Lift-Curve Slope," *Journal of Aircraft*, Vol. 34, No. 3, 1997, pp. 450–452.
doi:10.2514/2.2193
- [22] Johnston, H. S., and Hagerman, J. R., "Wind-Tunnel Investigation at Low Speed of the Lateral Control Characteristics of an Unswept Untapered Semispan Wing of Aspect Ratio 3.13 Equipped with Various 25-Percent-Chord Plain Ailerons," NACA TN 2199, Oct. 1950.